The Effects of Fiber Orientation and Adhesives on Tensile Properties of Carbon Fiber Reinforced Polymer Matrix Composite with Embedded Nickel-Titanium Shape Memory Alloys

Derek Quade[a,*], Sadhan Jana[b], Gregory Morscher[b], Manigandan Kannan[b], Linda McCorkle[c]

[a] Glenn Research Center, Cleveland, Ohio

[b] University of Akron, Akron, Ohio

[c] Ohio Aerospace Institute, Brook Park, Ohio

* Corresponding Author, Derek.J.Quade@nasa.gov

Abstract

Tensile tests of Nickel-titanium (NiTi) shape memory alloys (SMA) embedded within carbon fiber reinforced polymer matrix composite (CFRP/PMC) laminates were evaluated with simultaneous monitoring of modal acoustic emissions (MAE). Three different layup configurations utilizing two different thin film adhesives were applied to bond the materials. Ultimate tensile strengths, strains, and moduli were obtained along with cumulative AE energy of events and specimen failure location. Scanning electron microscopy was used to examine the break areas of the specimens post-test. Microscopy was used to validate failure locations revealed from MAE analysis. 90° plies in the outer ply gave the strongest acoustic signals as well as the cleanest fracture of the specimens tested. Overlapping 0° ply layers surrounding the SMA was found to be the best scenario to prevent failure of the specimen itself.

Keywords:

A. Shape Memory Alloy

B. Polymer Matrix Composite

C. Acoustic Emissions

D. Mechanical Testing

E.

1. Introduction

The use of shape memory alloys (SMAs) within composite materials has formed an active area of research in the past decade. The SMAs are able to generate large amounts of stress while embedded within composite structures if they are triggered by resistive heating or temperature change. Initial research efforts in this area focused on characterization of NiTi wires and NiTi strips within a variety of composites during activation [1-4]. The dynamics of SMA activation within composite materials is an active area of research, looking at 3-point bend and beam analysis [5], debonding mechanics during activation [6], as well as bending and twisting in simple composites [7] and more advanced plate composite structures [8,9]. Beyond basic mechanics, fabrication and implementation of NiTi chevrons has been accomplished [10], as well as a variety of actuators utilizing polymer composite materials embedded with SMAs [11-13]. All the aforementioned research is possible due to the functional property of the SMA based on the reversible, thermoelastic martensitic transition of the crystalline structure [14]. Austenitic crystals shift to a variety of martensitic configurations at the times of heating or loading and unloading. This shift in configuration is directly responsible for the generation of stresses within the materials when they are constrained in the composites [15]. The flexibility and stiffness of an actuator can be optimized by using different lay-ups within the composites, in relation to the placement of the SMAs in composite panels.

Prior research work focused on areas such as modeling the stresses within the PMC [10,12], enhancing the bond between SMA and the host composite [6,7,16], and full-scale application of the resultant SMA-PMC actuators [11-13]. In all cases, the interactions and optimization of the bonds between SMA and composite received significant attention [1-16]. A majority of experimental systems capitalized on optically clear systems, such as transparent glass [3] or aramid fibers [1,2,7,10] paired with optically clear resins. Optical methods, such as Raman spectroscopy, were used for monitoring of stress and debonding at the interfaces of two dissimilar materials [1,4,7,10,15]. Exceptions are carbon fiber reinforced polymers – CFRP's where the interactions between SMA's and PMC's could not be monitored with the above methods [16,17] due to opacity of the composite panels. As is evident, the research in this narrow area has focused

primarily on the interactions and processing of the SMA and CFRP with little to no focus on the effects of CFRP structure on how the SMA would respond under thermal trigger.

The goal of the present research is to examine the effects of bonding between the SMA and the PMC in the composite panels in the presence of an adhesive. In conjunction, the work focuses on how the structure of the CFRP influences the interfacial bond between SMA and PMC. For this purpose, three hybrid composite specimens with the same weight ratio of SMA and PMC but differing ply configurations were tested under tension. Two film adhesives were used to bond the SMA to the interior of the PMC. A control bond of the default PMC epoxy phase was tested as well. Tensile tests were performed while a trio of acoustic sensors were attached to the specimens to monitor the modal acoustic emissions (MAE) during failure. The MAE and mechanical data was compared to see if an optimal layup configuration exists within the PMC for crack/debonding monitoring of the SMA-PMC bond when failure occurs.

2. Experimental Procedure

The hybrid composite specimens investigated in this paper consisted of PMC laminates with interior sections of NiTi SMA. The PMC (HexPly 8552 Epoxy Matrix embedded with IM7 carbon fibers obtained from Hexcel) is a mid-toughened, high strength and damage-resistant structural epoxy matrix surrounding the IM7 carbon fibers. This material has a tensile strength of 111 MPa, a tensile modulus of 11.7 GPa, flexural yield strength of 1860 MPa, flexural modulus of 15.2 GPa, and shear strength of 115 MPa [18]. The SMA (flat annealed NiTi sheets supplied by Johnson Matthey), measured 457.2 mm in length, 101.6 mm in width, and 0.127 mm in thickness.

Assembly of the hybrid composite specimens started with preparation of the SMA material. Rectangular inserts were cut from the sheets measuring 25.4 mm in length, 101.6 mm in width and 0.127 mm in thickness. These inserts were cleaned with acetone, dried, and then placed within empty sections of single 0° ply laminates of the PMC. This single ply was then fabricated within 8 separate plies of PMC (4 above and below). Three different ply orientations of the upper and lower laminates were fabricated in order to investigate whether an optimal layup configuration exists to protect the inner SMA layer. Three

adhesive bonding scenarios were also pursued in this study. Two separate thin film adhesives, Hysol EA9696 [19] and FM 377U [20], were bonded directly to the NiTi inserts and compared to control specimens without added adhesives. The three layup configurations are shown in Fig. 1.

Specimens were assembled as 152.4 mm x 152.4 mm panels and cured within an autoclave following procedure specified for HexPly 8552 [18]. Specifically, the parts were first cured for 1 hours at 110° C under full vacuum and a pressure of 0.1 MPa. The temperature was then ramped up to 176° C and vacuum vented when the pressure increased beyond 0.2 MPa to a total pressure of 0.68 MPa for 2 hours. After processing, the panels were cut via water jet into 25.4 mm wide, 152.4 mm long parts for tensile testing, as schematically shown in Fig. 2. E-glass tabs measuring 25.4 mm x 25.4 mm were attached to the designated grip sections of the specimens using AF 163-2M film adhesive [21].

In order to investigate the tensile fracture properties of these systems, all specimens were subjected to tensile elongation according to ASTM D3039 method [22]. Testing was conducted at room temperature on an Instron 5582 universal testing machine at a cross head displacement of 1.27 mm/min. Three acoustic sensors were attached to the specimens at the center, 25.4 mm above, and 25.4 mm below the center line. Vacuum grease was used to secure solid body contact of the sensor with the test specimen. In addition, clips were used to secure the sensors to the specimen. The acoustic sensors were connected to a Digital Wave preamplifier, which in turn was connected to a computer running the WaveExplorer software suite (Digital Wave, Huntingdon Valley, PA). AE sampling was performed at a rate of 10 MHz, while 2048 data points for each waveform was recorded, including 512 per-trigger points. The correct placement of the AE sensors and the functioning of the sensors were checked by performing lead break tests. During testing, the load and displacement data was recorded from the Instron 5582 on one computer while the AE data was collected on a separate computer. Fig. 3 shows a test specimen with attached AE sensors.

3. Results and Discussion

The strength and stiffness of a composite depends on the orientation sequences of the plies [23]. A laminate with 0° plies is stiffest and strongest in regards to axial tensile loads while ±45 plies are stiffest and

strongest in regards to shear loads. A laminate with 90° plies is stiffest and strongest in regards to side loads. This is due to the fact that in a composite part, the fiber is the load carrying element; a composite material is only strong and stiff in the direction of the fibers. The matrix supports these fibers and bonds them together within the composite. It stands to reason that tensile failure in a quasi-isotropic layup, as was used in this study, would first occur in the ply layers made up of fibers in the 90° orientation. This will be shown via acoustic emission signals, microscopy, and specimen break patterns.

In this study, hybrid SMA/PMC composites have been fabricated, and the tensile fracture and acoustic emissive properties have been investigated. These specimens consisted of Hexcel 8552 polymer matrix composite laminates with embedded nickel-titanium shape memory alloy inserts. Tensile tests were conducted in order to investigate the adhesive properties of these specimens, which included differing thin film adhesives as well as different ply layups. Table 1 shows the tested specimens for this study. Specimens A-C consisted of control samples (omitting SMA from the central ply), specimens D-F consisted of laminates with SMA inserts without adhesive, specimens G-I represent samples with SMA bonded with Hysol EA9696 adhesive, and specimens J-L represent SMA samples bonded with FM 377U adhesive. Ply layup configurations follow the order presented in Fig. 1.

Fig. 4 shows a typical stress vs. strain curve of the first control series following tensile tests at 1.27 mm/min. All subsequent tensile tests showed similar results. From the figure, it is clear that the systems exhibited standard fracture and failure behavior of rigid PMC's in tensile mode. Despite an initial variation in the slope of the curve in Fig. 4, the specimen moduli were consistent and stable throughout the tests. After these plots were generated, an analysis of the mechanical data was performed based on the equations presented by ASTM standard D3039 [22]. The ultimate tensile strength values were calculated using:

$$F^{tu} = {P^{max}}/{A} \quad (1)$$

$$\sigma_i = {P_i}/{A} \quad (2)$$

where F^{tu} is the ultimate tensile strength (MPa), P^{max} is the maximum force before failure (N), σ_i is the tensile stress at the i-th data point (MPa), P_i is the force at the i-th data point (N), and A is the average cross-

sectional area (mm^2). The averages for each series are summarized in Fig. 5 for comparative analysis. Predictably, the hybrid composite specimen with the highest ultimate tensile strength (744.24 MPa) in Fig. 5 was a control series without an SMA insert; specifically, the control specimen containing a triple 0° ply layer at the center of the laminate. Looking at the standard deviation values within the control series, however, shows that these sets of tests were all statistically in the range with each other. The rest of the specimens with SMA strips did not show any type of patterns in ultimate tensile strength. In fact, the strongest specimen with SMA strip did not have additional adhesive, while the weakest specimen included adhesive. It can be summarized that the use of additional adhesives can actually be detrimental to the ultimate strength if proper adhesive selection and SMA surface treatment are not used.

As presented earlier, a trio of acoustic sensors were attached to each specimen before subjecting them to tensile tests. As the specimens underwent failure, acoustic events were recorded and marked at each time instant. The cumulative AE energy of events are plotted alongside stress for each of the test specimens to better correlate the acoustic signal with the mechanical failure events. A representative graph of this data is shown in Fig. 6. Acoustic signals detected can be directly attributed to breaks and cracking within the specimen during testing. Direct comparison of mechanical test data alongside cumulative AE signals show a correlation between increasing acoustic emissions and load drops within the mechanical test data, signifying a crack or break within the test specimen. Analysis of Fig. 6 also highlights both the start and extent of internal cracking within specimen B-1 at distinct times. Specimen micro-cracking begins at a test time of ~115 seconds (~1 MPa), when AE signals are first detected. As the test proceeds, large energy signatures throughout the specimen are noted to occur at ~190 seconds (~210 MPa), with the final failure sequence starting around ~210 seconds (~285 MPa) and ending at ~260 seconds (~900 MPa).

Analysis of AE data was continued after generation of cumulative AE plots. This was accomplished based on a set of equations developed by Morscher [24]. These equations are used to track the crack locations within tensile specimens based on acoustic measurements generated during failure. One such equation is presented below:

$$\text{Location} = \frac{x}{2} * \left(\Delta t / \Delta t_x\right) \quad (3)$$

where x is the distance between the two outer AE sensors, Δt is the arrival time of sensor A subtracted by the arrival time of sensor C (microseconds), and Δt_x is the outer position arrival time of sensor A subtracted by the arrival time of sensor C (microseconds). For this test setup, sensors A and C are the upper and lower most sensors on the specimen. The Wave Explorer software allows tracking of the specific times when the AE signals cross a particular sensor producing the values of Δt. In this regard, Δtx is the change in time between the outer sensors when an acoustic event takes place far *outside* the sensor locations. This is achieved during lead breaks, where an extensional wave, generated by the breaking of pencil lead on the sample is produced far outside the sensor locations. Using equation 3, AE events between sensors A and C can be accurately located.

Fig. 7 shows a plot of stress vs. time and acoustic signals generated during tensile testing. The AE signals shown in this graph, however, correlate to specific 2-dimensional locations on the specimen itself. For better reference, an image of the broken specimen (between sensor A and C) is placed alongside the graphs. Placement of the specimen image alongside the graph helps give definitive locations for cracks during tensile failure. These locations can also be correlated to the time as well as the stress present within the specimen when the acoustic energy from cracking was produced. Clusters of acoustic signals at part failure match where ultimate failure of the specimen occurred.

Along with the location plots shown above, stress vs AE energy plots inspired by Baker [25] were generated. In these plots, the stress is directly plotted against the cumulative AE energy of events. By manipulating the AE time data to match with specific time points of stress, the time axis seen in Fig. 7 can be removed, allowing a direct comparison of stress and acoustic energy. An example of the trend is shown in Fig. 8. The trends in Fig. 8 directly correlate the stress present in a tested system to the amount of acoustic energy recorded. This relationship is directly connected to the lay-up of the system. In Fig. 8, the A series lay-up generates significantly less acoustic energy in comparison to other lay-ups. The highest amount of acoustic energy generated during tensile testing is seen for the lay-up in the C series. This is due to the

location of the 90° plies within the specimen; the conclusion being that the closer the 90° plies are to the surface of the specimen, the larger the acoustic signal will be.

To further establish the relationship between ply orientation and AE signal strength, plots of AE failure correlated to the values of stress and time shown in Fig. 7 were improved upon by plotting the location of AE events along with identifying the "strength" of these events. This is shown in Fig. 9. For this figure, strength of AE signals was divided into three categories; small events (<1 V^2-sec), medium events (1-10 V^2-sec) and large events (>10 V^2-sec). Three different specimens, with 90° plies located at the center (specimen B-1), 90° located mid-way from center to exterior (specimen D-3), and 90° plies located on the specimen surface (specimen L-1). As was the case in Fig. 8, the placement of the 90° plies on the outside of the specimens maximizes the amount and strength of the AE signals generated. These changes in AE signal strength and amount can be explained by Modal Acoustic Emission theory, which has been previously applied to waveforms generated from a variety of events occurring throughout the mechanical failure of a PMC [25-29]. A surface crack will generate a low frequency flexural (antisymmetric) waveform due to a bending moment associated with an off-center crack. An interior 90 ply transverse crack will generate a high frequency extensional (symmetric) waveform, due to the axial-directed pressure associated with a 90 ply transverse crack that is near the center of the specimen.

Along with 2-dimensional location of the AE signals between the outer sensors, analysis of the waveform frequencies generated can reveal where cracking was initiated in a sample. As previously described, surface cracks will generate low frequency waveforms, while interior cracks will generate high frequency waveforms. By looking at the first and last waveforms generated during testing, it can be revealed whether the specimens began cracking from the interior or exterior. Fig. 10 shows waveforms generated at the beginning and end of testing for specimens B-1, D-3 and L-1. Image A shows one of the first waveforms generated during B-1 specimen testing, while image B shows one of the last waveforms generated during B-1 specimen testing. The majority of waveforms that first occurred within specimen B-1 were similar to image A; high frequency waveforms. The majority of waveforms that occurred near the end of testing of specimen B-1 were similar to image B; low frequency waveforms. The transition from high

frequency to low frequency wave form indicates that the initial cracks in specimen B-1 took place within the interior of the specimen, starting where the 90° plies were located.

The same case is shown for specimen D-3 in images C and D. The majority of waveforms to first occur within specimen D-3 were similar to image C; high frequency waveforms. The majority of waveforms to occur last within specimen D-3 were similar to image D; low frequency waveforms. Again, this change in frequency from high to low indicates that the initial cracks in specimen D-3 took place within the specimen, starting where the 90° plies were located.

Images E and F for specimen L-1 are opposite of the trends shown in images A-D in Fig. 10. In these images, low frequency waveforms occurred at the beginning of testing for specimen L-1, while high frequency waveforms occurred near the end of testing. Examination of the ply structure shows that specimen L-1 had 90° plies on the exterior. The transition from low frequency waveforms to high frequency waveforms shows that failure occurs starting at the outside of the specimen, where the 90° plies are located.

The effect of various CFRP layups and adhesive treatments were also examined via scanning electron microscopy after testing was complete. In these images, sections of the specimens are shown that were close to the bond failure lines, or where significant cracks were noticed on the specimen edges.

Scanning electron microscopy was performed on a Hitachi S-4700 electron microscope running at 6 kV voltage and average working distance of 12 mm from the detector. Images were taken at the edges of the crack areas as well as on the surface crack areas in order to highlight crack propagation at the break of the specimen (fracture) during crack propagation along the edges (delamination). These images are placed alongside both a macroscopic photograph of the specimen, along with the layup configurations. The individual plies within the panels are identified within the SEM images of the fracture surfaces. Fig. 11 and Fig. 12 represent the break patterns that occurred within the first layup series (+45/0/-45/90/0/90/-45/0/+45). Fig. 11 shows that delamination occurred between the lower 90° ply and -45° plies with little to no delamination seen elsewhere. Fig. 12 shows the variety of breaks along the many different plies; the 90°

ply underwent a clear break throughout the material. This emphasizes the importance of the 90° ply in fracture and delamination; the fracture occurred at the 90° ply first, and resulted in a delamination of the composite specimen.

Fig. 13 and 14 present the break patterns that occurred within the second layup series (+45/90/-45/0/0/0/-45/90/+45). Fig. 13 highlights the importance of placement of the 90° plies; delamination in this image runs between the ply layers in contact with the 90° plies. Further analysis shows the lack of delamination or cracks along the central triple 0° ply. This observation gives rise to the notion that an SMA insert embedded within this area would be least likely to cause an external failure at a 90° ply. A lack of visible plies within Fig. 14 highlights the fact that a break within the specimen will occur at a 90° ply and travel through the specimen as a delamination until the ultimate failure occurs within the midsection triple 0° plies.

Fig. 15 and 16 look at the break patterns that occurred within the third layup series (90/+45/0/-45/0/-45/0/+45/90). Fig. 15 highlights the random nature of the delamination when the break of the specimen occurs all in one area. Unlike the other specimens, delamination within the third layup series varies along several of the different plies. Fig. 16 highlights the "clean" break seen in this series; the break begins at the outer ply (90°) and travels quickly through the specimen. It is hypothesized that as the near instantaneous break occurs at this singular area, a variety of delamination also occur through the specimen. These delaminations vary in the ply layers that they occur within, but are smaller in comparison to the delaminations seen in layups 1 and 2, as shown in Fig. 11-14. The third layup proves to be a poor use for SMA implementation, as the random delaminations throughout the specimen occur at the very center, as well as outer plies.

4. Conclusion

This study examined the interaction between SMA adhesion with PMC's along with the effect that PMC lay-ups would have on this bonding. Three different bonding scenarios, along with three different lay-ups were utilized and tested in tensile modes. During testing, these specimens were monitored with

acoustic sensors; these AE signals were then plotted against the stresses in the systems along with break locations during sample failure.

Without any preparation of the SMA surfaces, the bond layer between PMC and SMA was not affected greatly by the addition of adhesives. There were no obvious trends in mechanical properties based on either the lay-up or adhesive used; the only real trend that occurred in data was more dependent on the presence of a triple layer of fibers oriented in the direction of the tensile force. The only downside to the triple layer of fibers was the explosive break that occurred during failure, which would result in a more difficult repair if this were an actuator in use. This central triple ply layer, however, was extremely resistant to delaminations caused by tensile forces; this would be an ideal use for SMA insertion within a PMC being loaded in some form of tension.

The behavior of the central SMA-embedded ply was (mechanically) the most important information derived from this study; follow up studies would likely compare how the fiber direction of the ply the SMA is embedded within differs mechanically. The insertion of an SMA capable of shape change within a PMC actuator may call for specifically oriented ply layers that the SMA is in line with. This, along with proper surface preparation and adhesives used would result in an SMA-PMC hybrid specimen capable of repeated actuation with minimal damage to the part.

Acoustic signals monitored during mechanical failure of specimens reacted as predicted by various other papers [25-29]; the presence of 90° plies (and their location within the various lay-ups) determined the amount and strength of cumulative AE energy detected during testing. AE location equations [24] were utilized in order to match acoustic signals along with specific times, stresses and locations on the parts. The frequency of AE wave data helped show whether failure began on the interior or exterior of the tested specimens. The overall data generated from AE analysis was successful in displaying where failure would occur in the part, no matter what lay-up configuration was used.

5. References

[1] Bollas, D: Stress Generation by shape memory alloy wires embedded in polymer composites. Acta Materiala 2007, 55, 5489-5499.

[2] Parthenios, J: Adaptive composites incorporating shape memory alloy wires. Composites: Part A 2001, 32, 1735-1747.

[3] Turner, T: Fabrication and Characterization of SMA hybrid composites. Smart Structures and Materials 2001, 343, 33-43.

[4] Hisaaki, T; Elzbieta, P; Yoshihiro, E; Toshimi, S: Thermomechanical Properties of Shape-Memory Alloy and Polymer and Their Composites. Mechanics of Advanced Materials and Structures 2009, 16, 236-247.

[5] Araujo, CJ: Fabrication and static characterization of carbon-fiber-reinforced polymers with embedded NiTiNOL shape memory wire actuators. Smart Materials and Structures 2008, 17, 6

[6] Poon, C; Zhou, L; Jin, W; Shi, S: Interfacial Debond of Shape Memory Alloy Composites. Smart Material Structures 2005, 14, 29-37.

[7] Schrooten, J: Progress on Composites with Embedded Shape Memory Alloy wires, Materials Transactions 2002, 43, 1-13.

[8] Kim, C; Park, B-S; Goo, N-S: Shape Changes by Coupled Bending and Twisting of Shape-Memory-Alloy Embedded Composite Beams. Smart Material Structures 2002, 11, 519-526.

[9] Ostachowicz, W: Dynamics and buckling of a multilayer composite plate with embedded SMA wires. Composite Structures 2000, 48, 163-167.

[10] Turner, T; Buehrle, R; Cano, R; Fleming, G: Modeling, fabrication, and testing of a SMA hybrid composite jet engine chevron concept. Journal of Intelligent Material Systems and Structures 2006, 17, 483-497.

[11] Song, G; Kelly, B; Agrawal, BN; Lam, PC; Srivatsan, TS: Application of shape memory alloy wire actuator for precision position control of a composite beam. Journal of Material Engineering Performance 2000, 9, 330-333.

[12] Lagoudas, DC: Modeling of a flexible beam actuated by shape memory alloy wires. Smart Material Structures 1997, 6, 265-277.

[13] Hebda, DA; White, S.R.: Structural behavior of SMA composite beams. Adaptive Material Systems 1995, 206, 111-119.

[14] Duering, TW; Melton, KN; Stockel, D: Engineering Aspects of Shape Memory Alloys. London: Butterworth-Heinemann, 1990.

[15] J.S.N, Paine; C.A., Rogers: Review of multi-functional SMA hybrid composites materials and their applications. Adaptive Structures and Composite Materials: Analysis and Application 1994, 54, 37-45.

[16] Xu, Y; Otsuka, K; Yoshida, H; Nagai, H; Oishi, R; Horikawa, H; Kishi, T: A New Method for Fabricating SMA/CFRP Smart Hybrid Composites. Intermetallics 2002, 10, 361-369.

[17] Jang, BK; Kishi, T: Thermomechanical Response of TiNi Fiber-Impregnated CFRP composites. Material Letters 2005, 59, 2472-2475.

[18] Hexply 8552; MSDS No. FTA 072e [Online]; Hexcel Composites, February 2013 http://www.hexcel.com/Resources/DataSheets/Prepreg-Data-Sheets/8552_eu.pdf (accessed May 2015).

[19] Loctite Hysol EA 9696; ID No. AF9118512 [Online]; Henkel Adhesives, April 2007 http://hybris.cms.henkel.com/henkel/msdspdf?matnr=698917&country=US&language=EN (accessed May 2015).

[20] Cytec FM 377U; ID No. AEAD-00014 [Online]; Cytec Adhesives, April 2010 http://www.cytec.com/sites/default/files/datasheets/FM_377_040710.pdf (accessed May 2015).

[21] 3M Scotch-Weld Structural Adhesive Film AF 163-2; ID No. 62319253092, November 2009 http://multimedia.3m.com/mws/media/282041O/3m-scotch-weld-structural-adhesive-film-af-163-2-af-163-3.pdf (accessed May 2015).

[22] ASTM D3039/D3039M – 08: Standard Test Method for Tensile Properties of Polymer Matrix Composite Materials.

[23] Pilato, L; Michno, M: Advanced Composite Materials, New York: Springer-Verlag Berling Heidelberg Publishing Company 1994.

[24] Morscher, G: Modal acoustic emission of damage accumulation in a woven SiC/SiC composite. Composites Science and Technology 1999, 59, 687-697.

[25] Baker, C; Morscher, M; Pumar, V; Lemanski, J; Transverse cracking in carbon fiber reinforced polymer composites: Modal acoustic emission and peak frequency analysis. Composites Science and Technology 2015, 116, 26-32.

[26] De Baere, I; Paepegem, WV; Quaresimin, M; Degrieck, J: On the tension-tension fatigue behavior of a carbon reinforced thermoplastic part I: Limitations of the ASTM D3039/D3479 standard. Polymer Testing 2011, 30, 625-632.

[27] Surgeon, M; Wevers, M: Modal analysis of acoustic emission signals from CFRP laminates. NDT&E International 1999, 32, 311-322.

[28] Prosser, WH; Jackson, KE; Kellas, S; Smith, BR; McKeon, J; Friedman, A: Advanced waveform based acoustic emission detection of matrix cracking in composites. NASA Langley Technical Report Server 1995.

[29] Gorman, MR: Modal AE: a new understanding of acoustic emissions. Journal of Acoustic Emission 1996, 14, 96-1002.

6. Figures

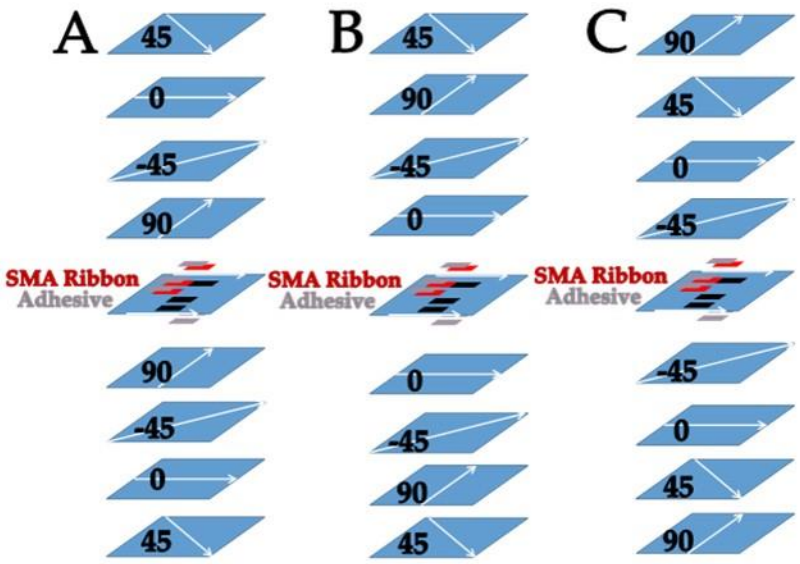

Fig. 1. Specimen Layup Configuration for Tensile Tests. Layup 1: (+45/0/-45/90/0/90/-45/0/+45) (A), Layup 2: (+45/90/-45/0/0/0/-45/90/+45) (B), Layup 3: (90/+45/0/-45/0/-45/0/+45/90) (C)

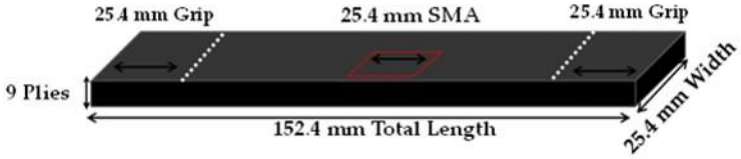

Fig. 2. Final specimen dimensions for tensile testing.

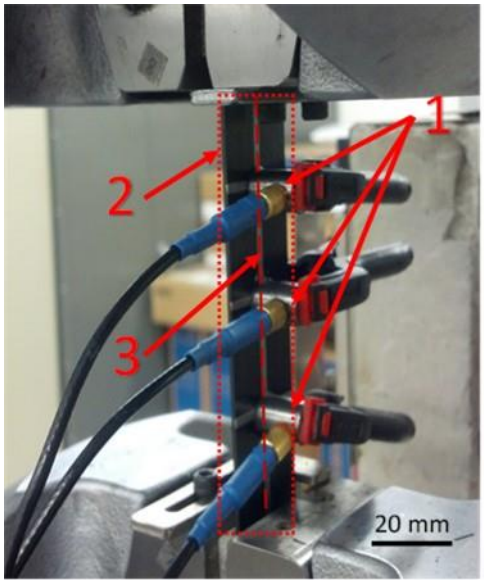

Fig. 3. Three Acoustic Sensors (1) mounted on Tensile Specimen (2) along center line (3)

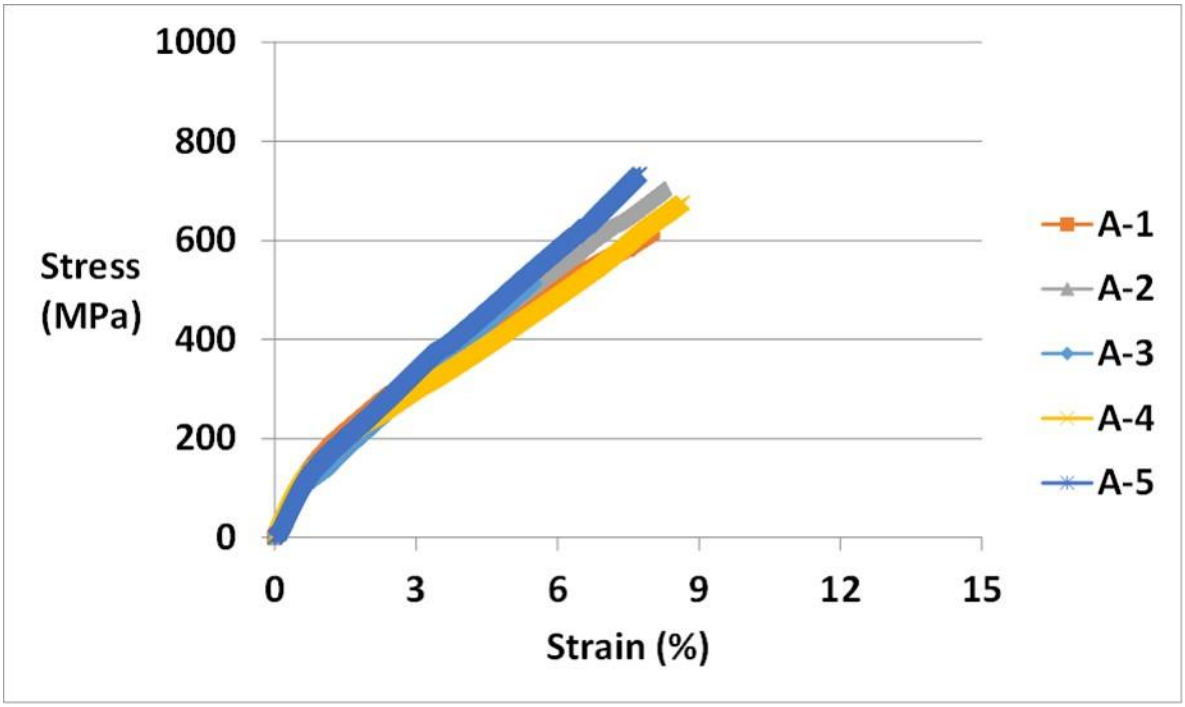

Fig. 4. Stress-Strain graph for Control Series A

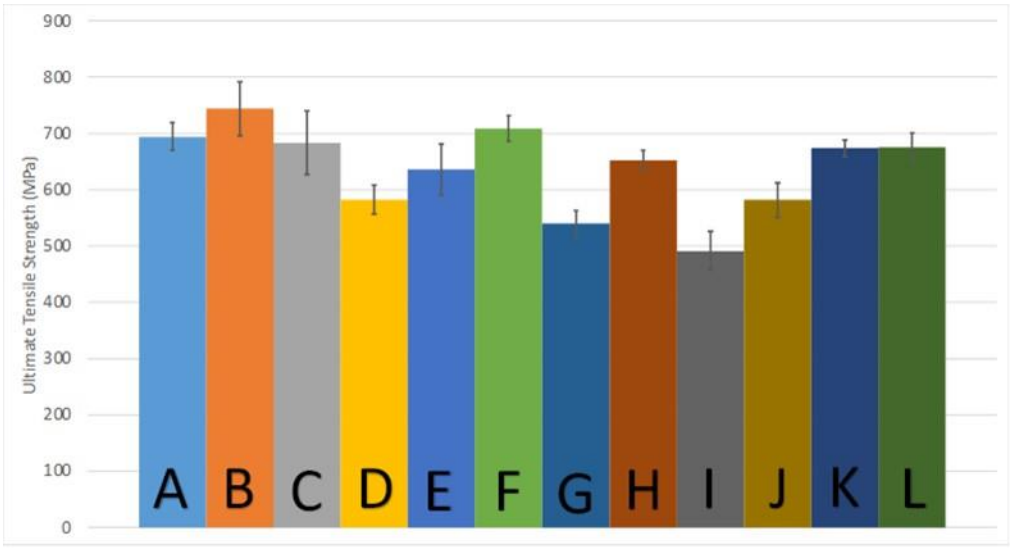

Fig. 5. Ultimate Tensile Strength of various specimens. A-C: Control, D-F: SMA control, G-I: SMA with Hysol Adhesive, J-L: SMA with FM Adhesive

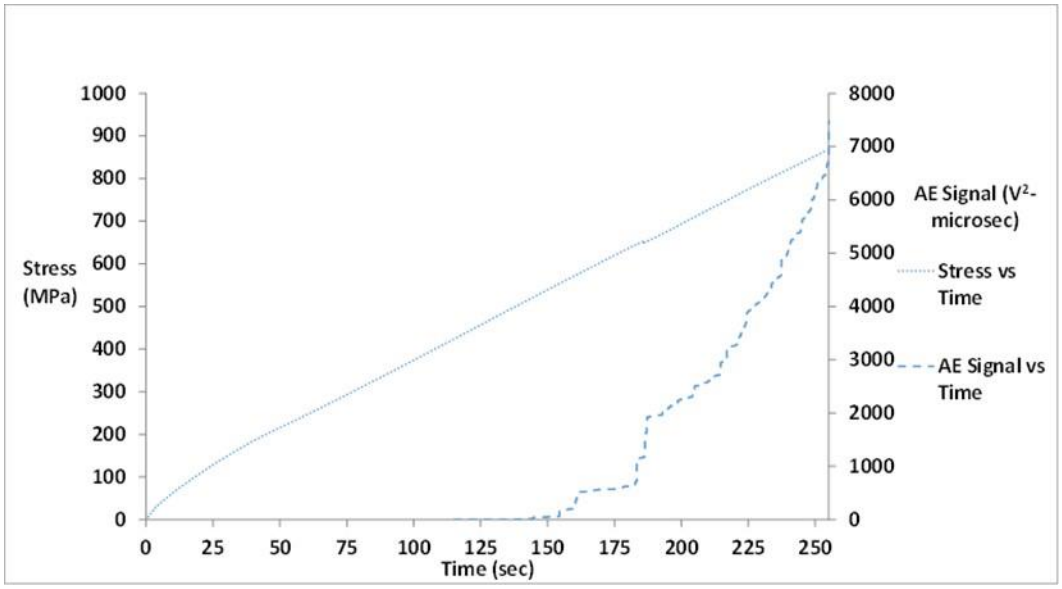

Fig. 6. Cumulative AE energy of events and stress plotted against time for specimen B-1.

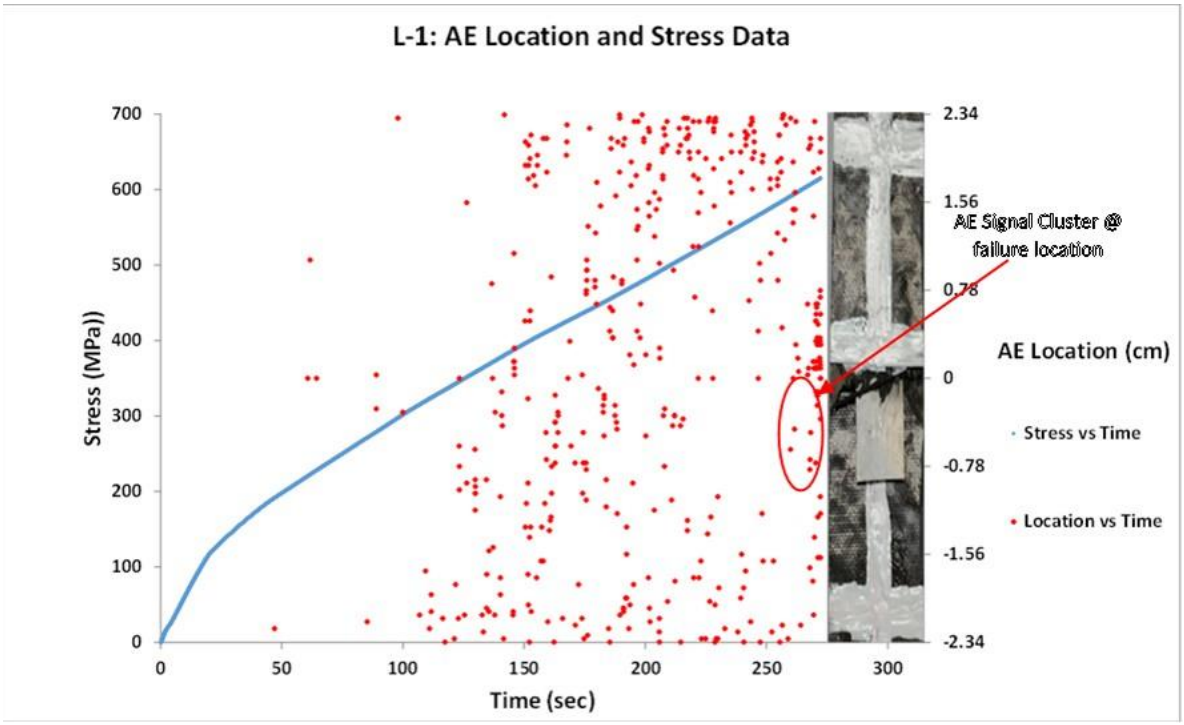

Fig. 7. Stress and AE Location plotted against time for specimen L-1

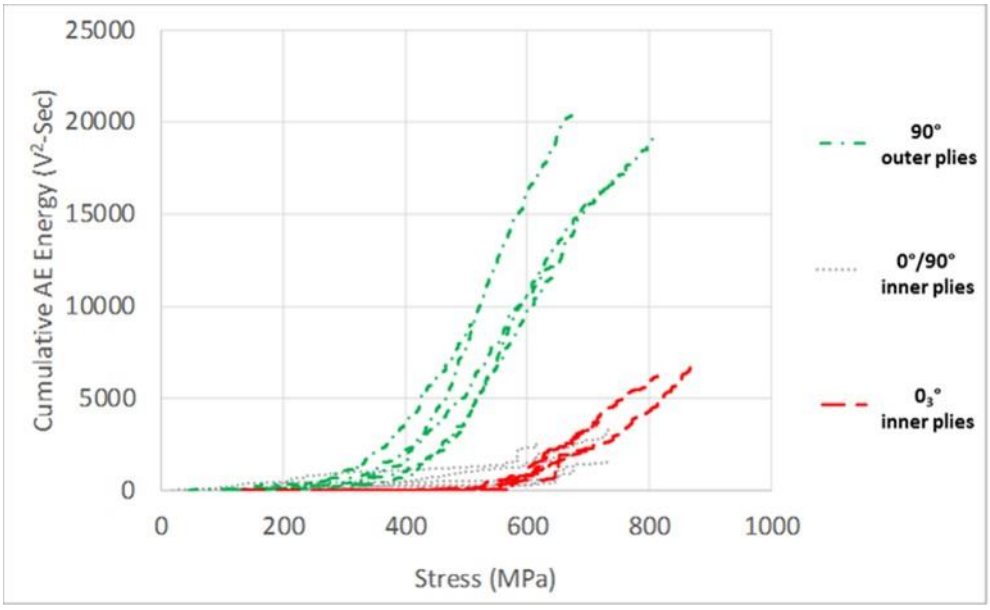

Fig. 8. Stress vs Cumulative AE Energy for Tensile Control series – Blue for lay-up 1, Red for lay-up 2, Green for lay-up 3

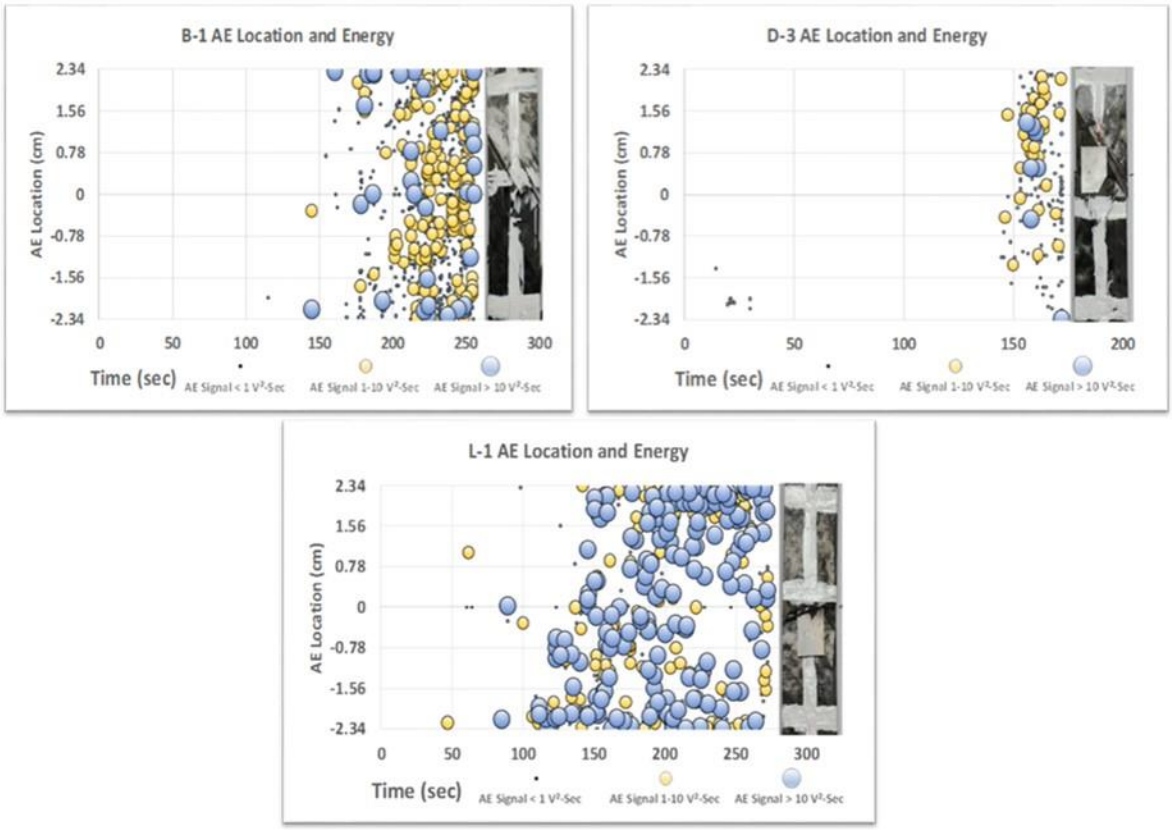

Fig. 9. AE strength and location plots for specimens B-1 (A), D-3 (B), and L-1 (C)

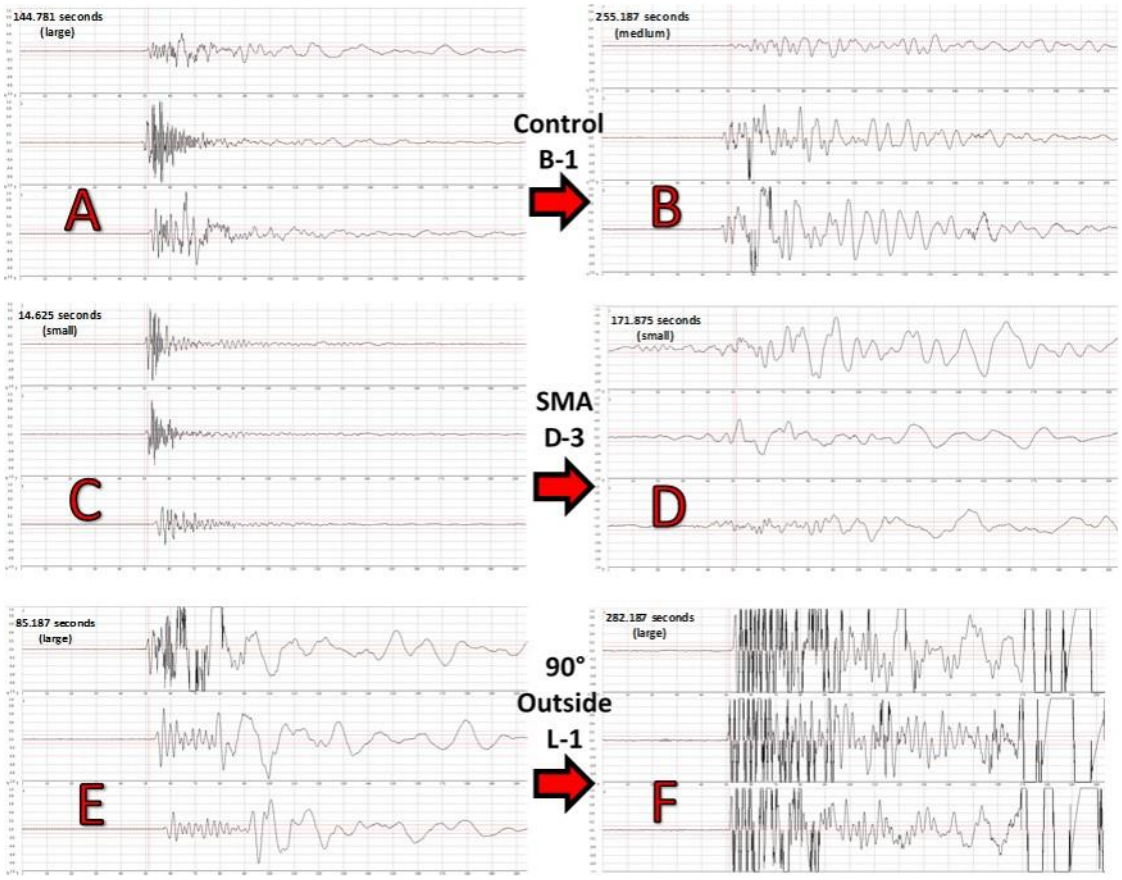

Fig. 10. Waveform frequencies for specimens B-1 (A,B), D-3 (C,D), and L-1 (E,F)

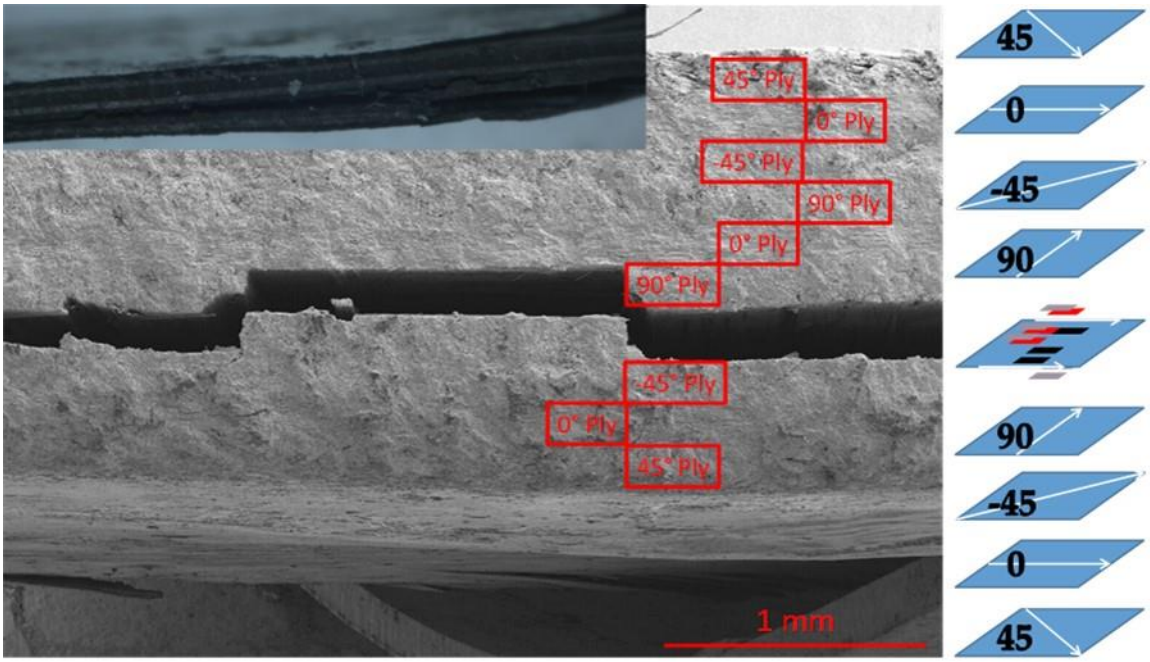

Fig. 11. Analysis of Ply Delamination Pattern in Layup 1 - (+45/0/-45/90/0/90/-45/0/+45)

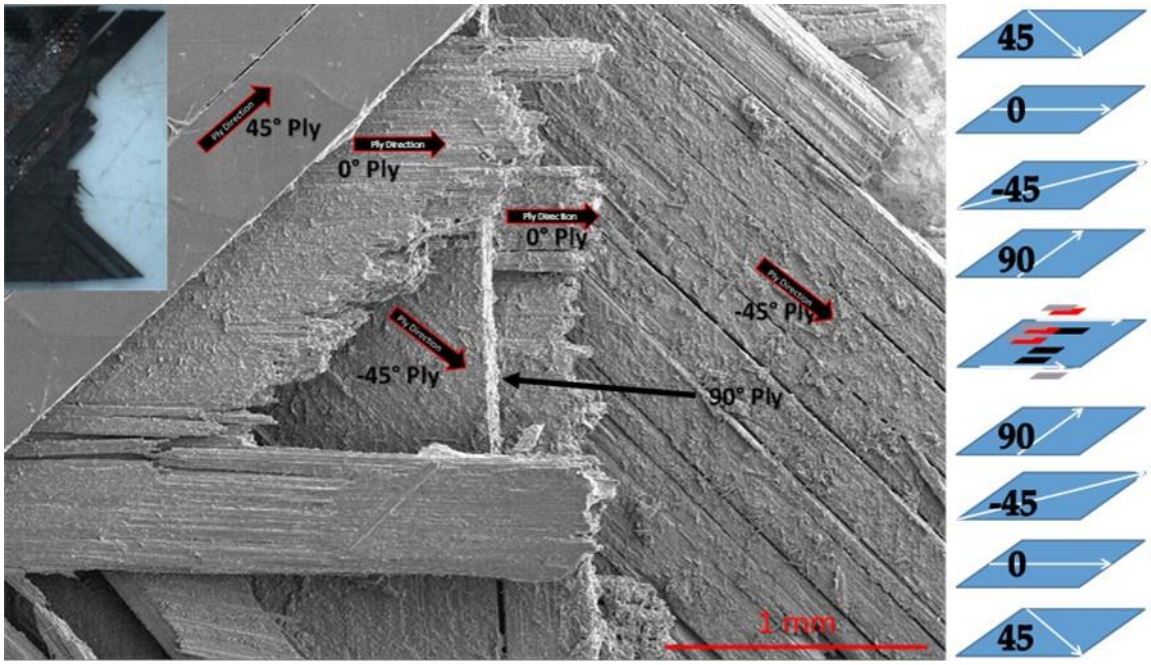

Fig. 12. Analysis of Ply Fracture Pattern in Layup 1 - (+45/0/-45/90/0/90/-45/0/+45)

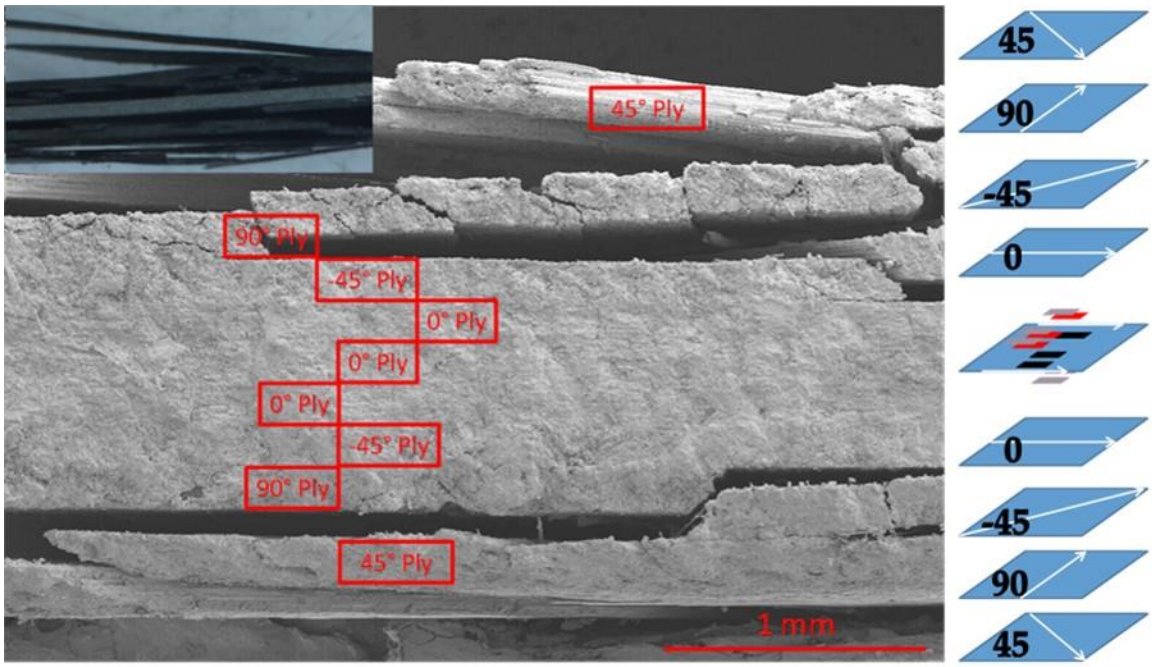

Fig. 13. Analysis of Ply Delamination Pattern in Layup 2 - (+45/90/-45/0/0/0/-45/90/+45)

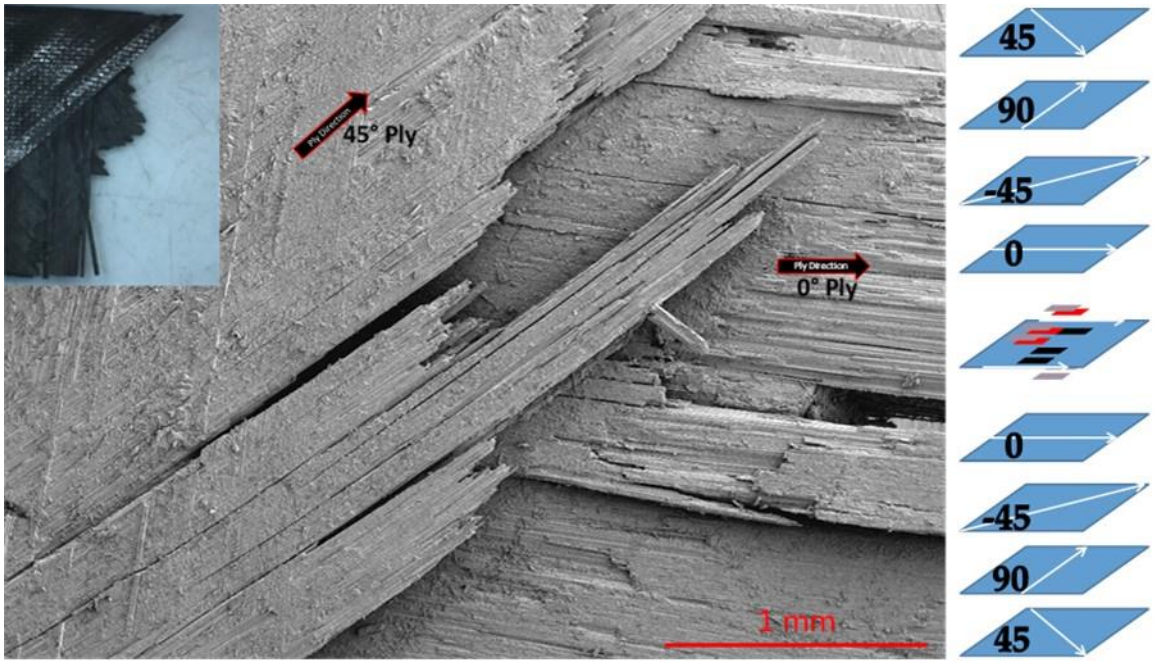

Fig. 14. Analysis of Ply Fracture Pattern in Layup 2 - (+45/90/-45/0/0/0/-45/90/+45)

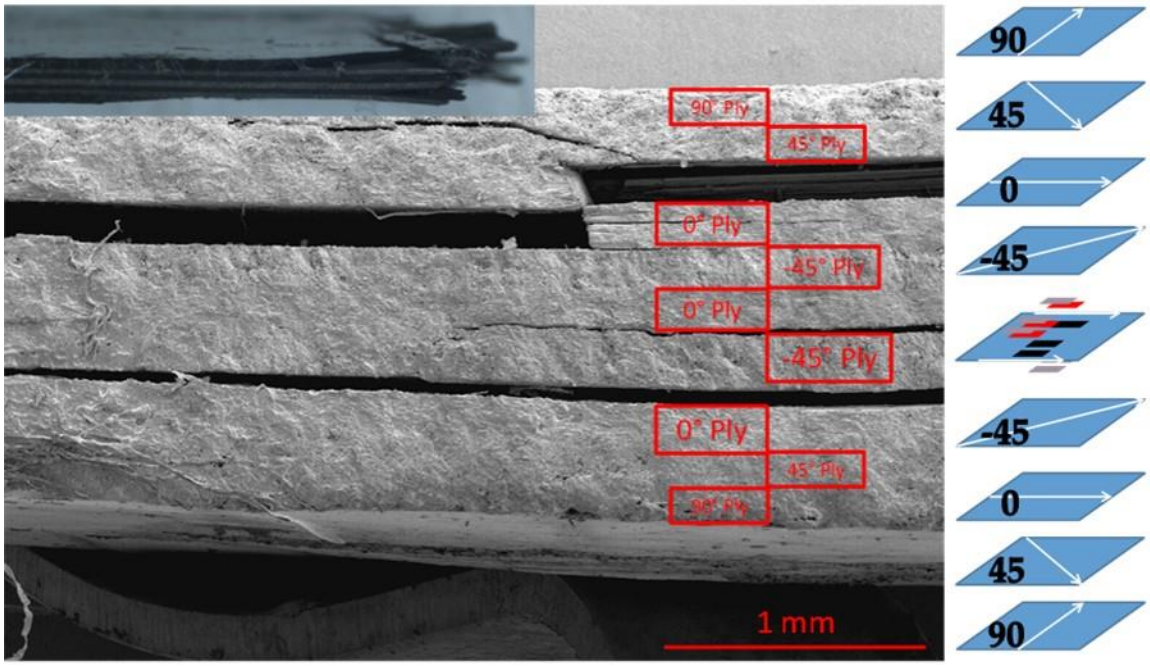

Fig. 15. Analysis of Ply Delamination Pattern in Layup 3 - (90/+45/0/-45/0/-45/0/+45/90)

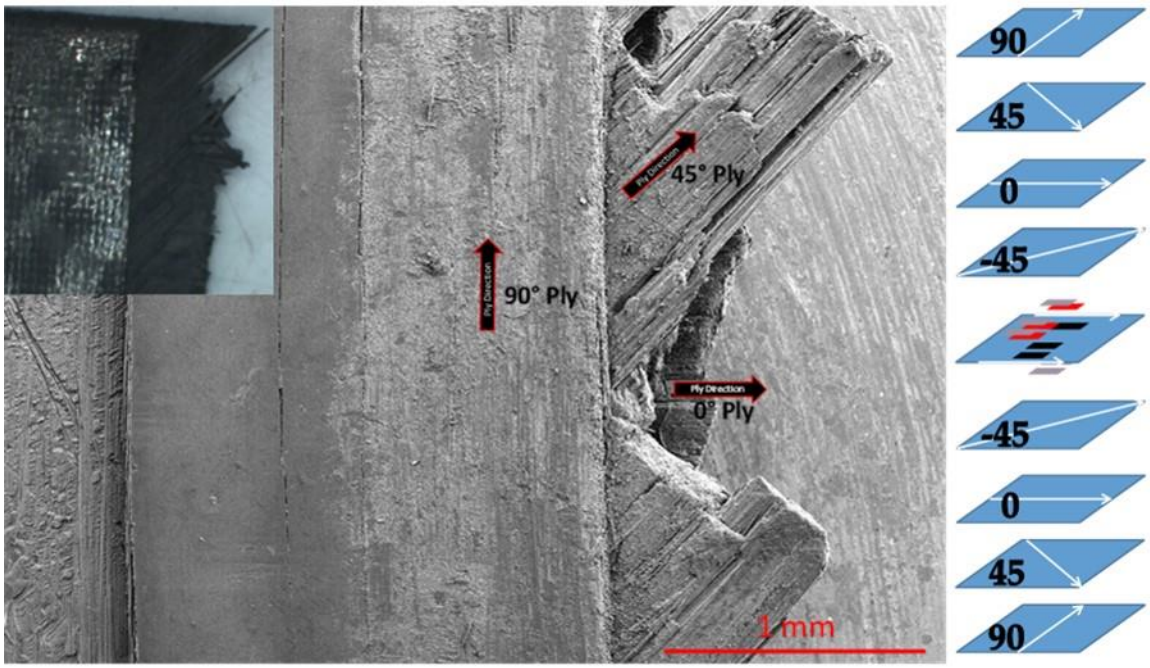

Fig. 16. Analysis of Ply Fracture Pattern in Layup 3 - (90/+45/0/-45/0/-45/0/+45/90)

7. Tables

Table 1

Tested Samples

Control Layup 1	Control Layup 2	Control Layup 3	SMA No Adh Layup 1	SMA No Adh Layup 2	SMA No Adh Layup 3	SMA Hysol Layup 1	SMA Hysol Layup 2	SMA Hysol Layup 3	SMA FM Layup 1	SMA FM Layup 2	SMA FM Layup 3
A-1	B-1	C-1	D-1	E-1	F-1	G-1	H-1	I-1	J-1	K-1	L-1
A-2	B-2	C-2	D-2	E-2	F-2	G-2	H-2	I-2	J-2	K-2	L-2
A-3	B-3	C-3	D-3	E-3	F-3	G-3	H-3	I-3	J-3	K-3	L-3
A-4	B-4	C-4	D-4	E-4	F-4	G-4	H-4	I-4	J-4	K-4	L-4
A-5	B-5	C-5	D-5	E-5	F-5	G-5	H-5	I-5	J-5	K-5	L-5
A-6	B-6	C-6	D-6	E-6	F-6	G-6	H-6	I-6	J-6	K-6	L-6